Eur. Phys. J. D **11**, 79–90 (2000)

THE EUROPEAN PHYSICAL JOURNAL D

EDP Sciences

Proton and electron impact on molecular and atomic oxygen: I. High resolution fluorescence spectra in the visible and VUV spectral range and emission cross-sections for dissociative ionisation and excitation of O_2

O. Wilhelmi and K.-H. Schartner[a]

I. Physikalisches Institut, Justus-Liebig-Universität, 35392 Giessen, Germany

Received 9 September 1999 and Received in final form 15 December 1999

Abstract. Molecular oxygen O_2 was dissociated in collisions with protons and electrons in the intermediate velocity range (p^+-energies: 17–800 keV, e^--energies: 0.2–2 keV). Fluorescence from excited atomic and singly ionised fragments and from singly ionised molecules was detected in the VUV and in the visible and near UV spectral range. Highly resolved spectra are presented for the VUV (46–131 nm) and the near UV/visible (340–605 nm) spectral range. Absolute emission cross-sections have been determined for dissociative ionisation and excitation leading to fluorescence in the VUV. Results are compared with published data.

PACS. 34. Atomic and molecular collision processes and interactions – 33.20.-t Molecular spectra

1 Introduction

Molecular oxygen O_2 as one major constituent of the earth's atmosphere is exposed not only to electromagnetic radiation from the sun, but also to collisions with electrons and protons. Due to photon absorption in the EUV and to particle impact, O_2 is partially dissociated. Densities of O_2 and O as well as characteristic energies of electrons and protons strongly depend on altitude in atmosphere [1]. Fluorescence spectroscopy of O_2 and O has shown to be a powerful tool for remote investigations of the earth's atmosphere [1,2]. In order to interpret fluorescence spectra from O_2/O-admixtures, emission cross-sections of radiative transitions following excitation and ionisation of O_2 and O are desirable. Highly resolved spectra and absolute emission cross-sections for electron and proton impact on O_2 are presented here. Fluorescence spectroscopy experiments concerning proton and electron impact on O are presented in paper II [3], while photoionisation of O and photodissociation of O_2 are described elsewhere [4,5].

Fluorescence emission in the VUV after electron impact on O_2 was intensively analysed in an experiment by Ajello and Franklin [6], who supplied the latest and most comprehensive spectroscopic data with respect to earlier studies [7–11]. Fluorescence emission in the VUV results from transitions in neutral or ionised dissociation fragments. Molecular fluorescence features have not been observed in this spectral range. We present a high resolution VUV spectrum which reveals intensity ratios of some close lying fluorescence lines, not resolved in the spectrum of Ajello and Franklin [6]. The high spectral resolution achieved in the visible and near UV allows an unambiguous identification of fluorescence lines from excited dissociation fragments. The absolute emission cross-sections of Ajello and Franklin [6] were determined for 200 eV electron impact on O_2 and emission cross-sections for four lines were presented in an electron energy range from threshold up to 400 eV. Our absolute emission cross-sections for 13 radiative transitions following dissociative ionisation and excitation expand the electron energy range to 2 keV. The only emission cross-sections for proton impact, known to the authors, were determined by Thomas and Bent [12] for the unresolved 441.5/441.7 nm line.

2 Experimental

2.1 Investigated processes

For the most prominent VUV fluorescence lines and some weak fluorescence lines belonging to processes of physical interest, absolute emission cross-sections have been determined in the present experiment. Experimental fluorescence wavelengths of the observed transitions and the respective electronic transitions are summarised in Table 1. The investigated dissociative ionisation and excitation processes are summarised in equations (1–3). Fluorescent fragments are designated by the excited electron or the produced vacancy (O ground state: $2s^2\ 2p^4\ {}^3\mathrm{P}^e$).

[a] e-mail: karl-heinz.schartner@exp1.physik.uni-giessen.de

Table 1. Fluorescence wavelengths and electronic transitions for the absolute emission cross-sections determined in this study.

Fluorescence wavelength	Electronic transition
dissociative 2s-electron ionisation	
83.3 nm	O^+: $2s2p^4\ ^4P^e \rightarrow 2s^22p^3\ ^4S^o$
58.1 nm	O^+: $2s2p^4\ ^2P^e \rightarrow 2s^22p^3\ ^2P^o$
53.8 nm	O^+: $2s2p^4\ ^2P^e \rightarrow 2s^22p^3\ ^2D^o$
71.9 nm	O^+: $2s2p^4\ ^2D^e \rightarrow 2s^22p^3\ ^2D^o$
79.7 nm	O^+: $2s2p^4\ ^2D^e \rightarrow 2s^22p^3\ ^2P^o$
64.4 nm	O^+: $2s2p^4\ ^2S^e \rightarrow 2s^22p^3\ ^2P^o$
dissociative ion excitation	
53.9 nm	O^+: $2s^22p^2(^3P^e)3s\ ^4P^e \rightarrow 2s^22p^3\ ^4S^o$
61.7 nm	O^+: $2s^22p^2(^3P^e)3s\ ^2P^e \rightarrow 2s^22p^3\ ^2D^o$
67.3 nm	O^+: $2s^22p^2(^3P^e)3s\ ^2P^e \rightarrow 2s^22p^3\ ^2P^o$
dissociative excitation	
79.2 nm	O: $2s2p^5\ ^3P^o \rightarrow 2s^22p^4\ ^3P^e$
87.9 nm	O: $2s^22p^3(^2P^o)3s\ ^3P^o \rightarrow 2s^22p^4\ ^3P^e$
98.9 nm	O: $2s^22p^3(^2D^o)3s\ ^3D^o \rightarrow 2s^22p^4\ ^3P^e$
99.9 nm	O: $2s^22p^3(^2P^o)3s\ ^1P^o \rightarrow 2s^22p^4\ ^1D^e$
102.7 nm	O: $2s^22p^3(^4S^o)3d\ ^3D^o \rightarrow 2s^22p^4\ ^3P^e$

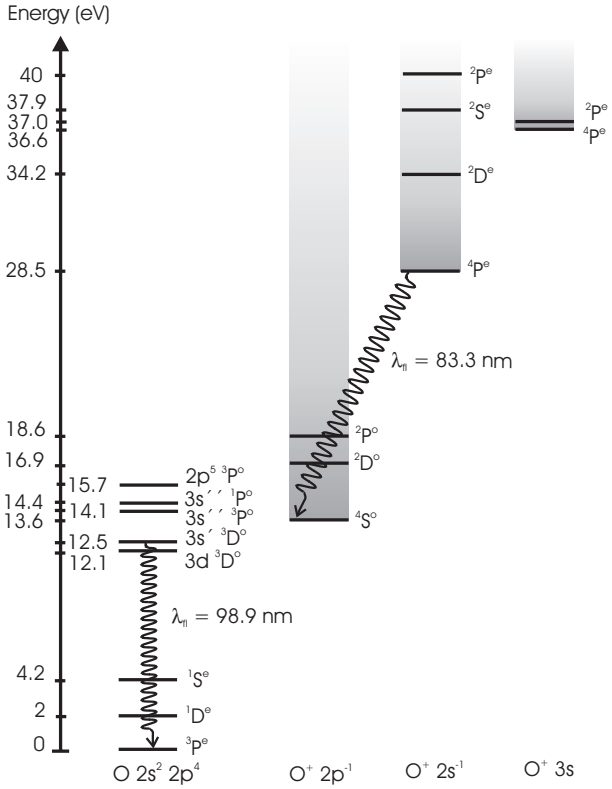

Fig. 1. Energy levels of O states and O^+ states with their continua which are relevant to VUV fluorescence emission. Two examples of radiative transitions are illustrated.

Complete designation as in Table 1 is omitted here. $h\nu_{\rm fl}$ symbolizes the emitted photon, $O/(O^+ + e^-)$ an unobserved fragment. Figure 1 illustrates the atomic and ionic states involved in the VUV emitting transitions.

Dissociative $2s-$electron ionisation:

$$\begin{array}{c} e^-,\ p^+ + O_2 \\ \downarrow \\ e^-,\ p^+ + O/(O^+ + e^-) + O^+\ (2s^{-1}) + e^- \\ \downarrow \\ O^+\ (2p^3) + h\nu_{\rm fl} \end{array} \quad (1)$$

dissociative ion excitation:

$$\begin{array}{c} e^-,\ p^+ + O_2 \\ \downarrow \\ e^-,\ p^+ + O/(O^+ + e^-) + O^+\ (3s) + e^- \\ \downarrow \\ O^+\ (2p^3) + h\nu_{\rm fl} \end{array} \quad (2)$$

dissociative excitation:

$$\begin{array}{c} e^-,\ p^+ + O_2 \\ \downarrow \\ e^-,\ p^+ + O/(O^+ + e^-) + O\ (3\ell \text{ or } 2p^5) \\ \downarrow \\ O\ (2p^4)\ + h\nu_{\rm fl}. \end{array} \quad (3)$$

In the visible and near UV spectral range, emission in the first and second negative band system of O_2^+ is observed along with fluorescence lines from excited dissociation fragments. The electron configuration of the molecular oxygen ground state is $O_2(X\ ^3\Sigma_g^+)$. Equations (4–6) summarise the fluorescent processes considered here.

1st & 2nd negative band system of O_2^+:

$$\begin{array}{c} e^-,\ p^+ + O_2 \\ \downarrow \\ e^-,\ p^+ + O_2^+\ (b\ ^4\Sigma_g,\ A\ ^2\Pi_u) + e^- \\ \downarrow \\ O_2^+\ (a\ ^4\Pi_u,\ X\ ^2\Pi_g) + h\nu_{\rm fl} \end{array} \quad (4)$$

dissociative ionisation:

$$\begin{array}{c} e^-,\ p^+ + O_2 \\ \downarrow \\ e^-,\ p^+ + O/(O^+ + e^-) + O^+\ (n\ell, n = 3, 4) + e^- \\ \downarrow \\ O^+\ (n(\ell \pm 1), n = 3) + h\nu_{\rm fl} \end{array} \quad (5)$$

dissociative excitation:

$$\begin{array}{c} e^-,\ p^+ + O_2 \\ \downarrow \\ e^-,\ p^+ + O/(O^+ + e^-) + O\ (n\ell, n = 3, 4, 5) + e^- \\ \downarrow \\ O(n(\ell \pm 0, 1), n = 3) + h\nu_{\rm fl}. \end{array} \quad (6)$$

2.2 Setup for measuring high resolution fluorescence spectra

Molecular oxygen was kept under a constant pressure of 5 mtorr in a target cell, giving a uniform target density of approximately 2×10^{14} cm^{-3} over the interaction region. Electrons of 2 keV kinetic energy passed the target cell through two apertures, each 1.5 mm in diameter. Fluorescence radiation was dispersed by a 1-m normal-incidence monochromator (Mc Pherson 225) mounted with its optical axis perpendicular and with its entrance slit parallel to the electron beam. The slit width was set to 100 μm.

In case of fluorescence detection in the VUV spectral range (46–131 nm), a platinum coated grating with 2400 lines per mm, blazed at 80 nm, was used. A two dimensional position sensitive channel-plate detector with an active area diameter of 2 inch registered a spectral range of about 18 nm simultaneously. A spectral resolution of 0.15 nm FWHM was achieved. Detected fluorescence intensities have been corrected for the relative spectral quantum efficiency of the present grating detector combination [13].

In case of fluorescence detection in the near UV and visible spectral range (340–605 nm), an aluminium coated grating with 600 lines per mm, blazed at 300 nm, was employed. A two dimensional position sensitive channel-plate detector with a multialkali photocathode (1 inch in diameter) registered a spectral range of about 30 nm simultaneously. The spectral resolution achieved here was 0.3 nm FWHM. The window material of the detector head prevented fluorescence detection at wavelengths below 340 nm.

In both cases spectra have been recorded for several settings of the gratings. Normalisation of the fluorescence intensity to the exciting electron beam current allowed to join the measured spectra. Wavelength calibration was carried out according to wavelengths compiled by Kelly [15], Striganov and Sventitskii [16] and Krupenie [17].

2.3 Setup for measuring absolute emission cross-sections

For determination of VUV emission cross-sections, a different experimental arrangement was set up in preparation of fluorescence spectroscopy experiments with atomic oxygen (paper II, [3,4]). Molecular oxygen was provided by an effusive beam which was formed by a nozzle (0.8 mm in diameter, 3 mm long). The mass flow of O_2 was electronically controlled. The molecular beam was intersected by the projectile beam. The intersection position 3 mm below nozzle exit was defined by five aligned circular apertures, the smallest one being 2.5 mm in diameter. The apertures were electrically insulated in order to monitor the position of the projectile beam by the currents from the apertures. The non-uniform target density was simulated in the intersection region on the basis of an effusive beam description by Pauly [18]. The mean density amounted to 5×10^{13} cm^{-3} for a typical mass flow of 1 sccm O_2. Protons with energies between 17 keV and 800 keV were provided by a 1 MeV van de Graaff accelerator, while for the production of 200 eV–2 keV electrons a modified TV electron gun was used. For the electron impact measurements, magnetic stray fields had to be screened.

A 1-m normal-incidence monochromator was mounted under the magic angle to the projectile beam in order to suppress the influence of anisotropic fluorescence emission on intensity detection. Its entrance slit was oriented perpendicular to the projectile beam. In order to compensate for the reduced target density in the effusive beam a 1200 lines per mm grating was chosen instead of the 2400 lines per mm grating which was used for the measurement of the high resolution VUV spectrum. Still supplying sufficient spectral resolution this grating allowed to register a spectral range of 36 nm simultaneously. The grating is osmium coated and blazed at 60 nm. The relative spectral quantum efficiency was obtained from fluorescence line intensities measured with Ar and Kr effusive beams under 2 keV electron impact. For this purpose, fluorescence intensity ratios were compared to accurate emission cross-section ratios by Jans *et al.* [19].

Absolute emission cross-sections have been obtained by comparing – under the same experimental conditions – the intensities of VUV fluorescence lines with fluorescence intensities emitted after Ar $3s$-electron ionisation with 2 keV electrons or with 300 keV and 800 keV protons. The fluorescence wavelengths emitted in the Ar^+ ($3p \rightarrow 3s$) transitions are 93.2 nm and 92.0 nm. Reference emission cross-sections from Jans *et al.* [19] for electron impact and Hippler and Schartner [21] for proton impact exist. Equal mass flow of Ar and O_2 was chosen. The target density for Ar is then by a factor 1.1 higher than that of O_2, because of the lower particle velocity of Ar due to its greater mass. This density difference was taken into account in the normalisation.

The deduction of the target density difference of a factor 1.1 between Ar and O_2 from their masses requires the effusive beam to be operated in the molecular flow regime. Whether or not molecular flow was achieved in the experiment was verified by applying the effusive beam simulation for comparison of experimental fluorescence intensities with simulated target densities for different mass flows. The simulation accounts for collisions in the nozzle and molecular flow in the beam itself (opaque mode) [18]. It has to be stated here, that the mass flow of 1 sccm in the present experiment is just beyond the validity of the simulation according to [18]. Reducing the mass flow to 0.25 sccm and 0.06 sccm (within the validity of the simulation), resulted in a simulated density reduction of 0.28 and 0.05 with respect to 1 sccm. Only a marginal reduction in the effusive beam diameter was obtained with decreasing mass flow. Experimentally, proton impact induced relative fluorescence intensities of 1:0.53:0.28 were measured for mass flows 1, 0.5 and 0.25 sccm. The agreement of the ratios of massflow and of fluorescence intensity with the simulated density ratio supports the application of the simulation program. It does also show the absence of pressure effects, like reabsorption of fluorescence by molecules. The simulation confirmed the factor 1.1 between Ar and

O_2 target densities which was expected assuming molecular flow conditions.

The reliability of the normalisation was supported by an additional experiment, where fluorescence was measured from diffuse O_2 and Kr targets of the same density under 2 keV electron impact. The 83.3 nm line (Eq. (1)) and 87.9 nm line (Eq. (3)) intensities from the diffuse O_2 target were normalised to accurate emission cross-sections of fluorescence lines emitted from excited Kr^+ states [19]. The 83.3 nm line emission cross-section for 2 keV electron impact obtained from the effusive beam amounts to 0.47 Mb, from the diffuse target experiment 0.43 Mb resulted. The 87.9 nm line emission cross-section of 0.14 Mb determined in the effusive beam experiment is in accord with 0.12 Mb from the diffuse target experiment.

2.4 Experimental uncertainties

The statistical errors of the emission cross-sections correspond to the number of counts registered for the individual fluorescence intensities. Furthermore a statistical variation in the overlap of effusive beam and projectile beam for different projectile energies had to be taken into account. The resulting statistical errors were determined by simulating different overlaps (simulation based on [18]). From the magnitude of the recorded aperture currents it could be concluded that only minor changes in projectile beam position had to be simulated.

Normalisation of the experimental fluorescence intensities to absolute emission cross-sections for the Ar^+ ($3p \rightarrow 3s$) transition causes systematic error bars. An error of 2.8% is reported for the reference cross-sections from the electron collision experiment performed by Jans *et al.* [19]. The absolute emission cross-sections from the proton collision experiment of Hippler and Schartner [21] are uncertain within 25%. The systematic error of the relative quantum efficiency correction was determined to be 23%. A possible different overlap of effusive beam and projectile beam in the measurements used for normalisation causes a further systematic error of 8%, also determined by simulating different overlaps.

All systematic errors add up to a total systematic error of 34% in case of the electron impact experiments and 56% in case of the proton impact experiments. The respective root sum square uncertainties are 25% and 35%.

3 Results and discussion

3.1 High resolution spectrum in the VUV (46–131 nm)

The VUV spectrum for collisions of 2 keV electrons with O_2 is displayed in Figure 2. The observed emission lines result from dissociation into ioniSed and excited O, O^+ and even O^{2+} fragments. Their transitions and wavelengths are listed in Table 2. Fine structure multiplets, even if partially resolved, are not listed separately for the sake of brevity. The assignment has been carried out using the

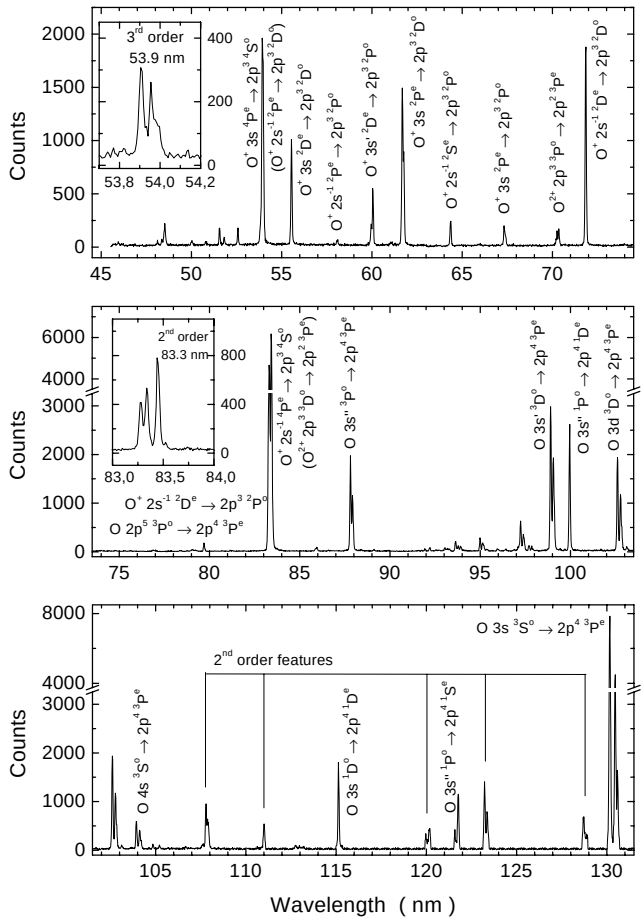

Fig. 2. The VUV spectrum resulting from 2 keV electron impact on O_2. Prominent emission features are designated by their corresponding electronic transitions. All emission features identified clearly are listed in Table 2. The insets show fluorescence spectra measured in higher diffraction orders.

wavelength tables of Kelly [15]. The achieved spectral resolution of 0.15 nm FWHM allows to investigate the intensity ratios of close lying fluorescence lines. The absence of any molecular emission features in this spectral region is obvious.

Fluorescence from O^+ ($2s^{-1}\ ^4P^e$) at 83.3 nm is overlapping with fluorescence from O^{2+} ($2p^3\ ^3D^o$) as can be seen in Table 2. To clarify the origin of fluorescence emission in this narrow spectral region, it has been measured with increased resolution in the second diffraction order of the grating as illustrated in the inset of Figure 2. The fluorescence intensity from O^{2+} at 83.5096 nm and 83.5292 nm can be distinguished from the O^+ fluorescence at 83.4462 nm. From the weak intensity of O^{2+} fluorescence emission, one can estimate the error to be less than 5% when fluorescence intensity at 83.3 nm is totally attributed to O^+ fluorescence emission in an experiment with lower resolution at comparable projectile energies.

The emission lines resulting from O^+ ($3s'\ ^2D^e$) at 60.0585 nm and O^{2+} ($2p^3\ ^1P^o/^1D^o$) at 59.7818/59.9598 nm are resolved in the first order of the spectrum. In contrast to the emission at 83.3 nm,

Table 2. Observed electronic transitions with corresponding fluorescence wavelengths in the VUV after dissociative ionisation into an excited fragment state. Fluorescence wavelengths are taken from Kelly [15]. Finestructure multiplets are summarised.

Observed transition	Fluorescence wavelength
fluorescence from excited O^{2+} fragments	
$3s\ ^3P^e \rightarrow 2p^3\ ^3P^o$	48.0955–48.1587 nm
$2p^3\ ^3S^o \rightarrow 2p^2\ ^3P^e$	50.7391–50.8182 nm
$2p^3\ ^1P^o \rightarrow 2p^2\ ^1D^e$	52.5795 nm
$2p^3\ ^1P^o \rightarrow 2p^2\ ^1S^e$	59.7818 nm
$2p^3\ ^1D^o \rightarrow 2p^2\ ^1D^e$	59.9598 nm
$2p^3\ ^3P^o \rightarrow 2p^2\ ^3P^e$	70.2332–70.3850 nm
$2p^3\ ^3D^o \rightarrow 2p^2\ ^3P^e$	83.2927–83.5292 nm
fluorescence from excited O^+ fragments	
$3d\ ^2D^e/^2P^e \rightarrow 2p^3\ ^2D^o$	48.1587–48.5631 nm
$3d\ ^2F^e/^4D^e \rightarrow 2p^3\ ^2D^o$	48.1587–48.5631 nm
$4s\ ^2P^e \rightarrow 2p^3\ ^2P^o$	49.9871–50.0343 nm
$3d\ ^2D^e \rightarrow 2p^3\ ^2P^o$	51.5498–51.5640 nm
$3d\ ^2P^e \rightarrow 2p^3\ ^2P^o$	51.7937–51.8242 nm
$2s^{-1}\ ^2P^e \rightarrow 2p^3\ ^2D^o$	53.7830–53.8318 nm
$3s\ ^4P^e \rightarrow 2p^3\ ^4S^o$	53.9086–53.9853 nm
$3s'\ ^2D^e \rightarrow 2p^3\ ^2D^o$	55.5056–55.5121 nm
$2s^{-1}\ ^2P^e \rightarrow 2p^3\ ^2P^o$	58.0400–58.0967 nm
$3s'\ ^2D^e \rightarrow 2p^3\ ^2P^o$	60.0585 nm
$3s\ ^2P^e \rightarrow 2p^3\ ^2D^o$	61.6291–61.7051 nm
$2s^{-1}\ ^2S^e \rightarrow 2p^3\ ^2P^o$	64.4148 nm
$3s\ ^2P^e \rightarrow 2p^3\ ^2P^o$	67.2948–67.3768 nm
$2s^{-1}\ ^2D^e \rightarrow 2p^3\ ^2D^o$	71.8484–71.8562 nm
$2s^{-1}\ ^2D^e \rightarrow 2p^3\ ^2P^o$	79.6661 nm
$2s^{-1}\ ^4P^e \rightarrow 2p^3\ ^4S^o$	83.2762–83.4462 nm
fluorescence from excited O fragments	
$2p^5\ ^3P^o \rightarrow 2p^4\ ^3P^e$	79.15136–79.29671 nm
$5d'\ ^1F^o/^1D^o/^1P^o \rightarrow 2p^4\ ^1D^e$	85.931–86.156 nm
$6s'\ ^1D^o \rightarrow 2p^4\ ^1D^e$	85.931−86.156 nm
$3s''\ ^3P^o \rightarrow 2p^4\ ^3P^e$	87.77983−87.95507 nm
$5, 6, 7, ...d\ ^3D^o \rightarrow 2p^4\ ^3P^e$	91.8039−95.07327 nm
$3d'\ ^1P^o/^1D^o/^1F^o \rightarrow 2p^4\ ^1D^e$	92.20081−92.2460 nm
$6, 7, 8, ...s\ ^3S^o \rightarrow 2p^4\ ^3P^e$	93.02566−95.29413 nm
$4s'\ ^1D^o \rightarrow 2p^4\ ^1D^e$	93.51930 nm
$4d\ ^3D^o \rightarrow 2p^4\ ^3P^e$	97.17381−97.38852 nm
$5s\ ^3S^o \rightarrow 2p^4\ ^3P^e$	97.64481−97.79594 nm
$3s'\ ^3D^o \rightarrow 2p^4\ ^3P^e$	98.85778−99.08010 nm
$3s''\ ^1P^o \rightarrow 2p^4\ ^1D^e$	99.94974 nm
$3d\ ^3D^o \rightarrow 2p^4\ ^3P^e$	102.57618−102.81571 nm
$4s\ ^3S^o \rightarrow 2p^4\ ^3P^e$	103.92304−104.16876 nm
$4s\ ^5S^o \rightarrow 2p^4\ ^3P^e$	104.9115 nm
$3s'\ ^1D^o \rightarrow 2p^4\ ^1D^e$	115.21512 nm
$3s''\ ^1P^o \rightarrow 2p^4\ ^1S^e$	121.76477 nm
$3s\ ^3S^o \rightarrow 2p^4\ ^3P^e$	130.21685−130.60286 nm

the fluorescence from O^{2+} is contributing significantly at 60 nm.

Only those emission features of O^{2+}, tabulated as the most intense in [15,16], appear in the VUV spectrum. So, in general one can consider the dissociation of O_2 into a doubly ionised excited fragment as significantly weaker than the dissociation into a singly ionised fragment, but care has to be taken, when weak emission lines of O^+ coincide with one of the observed O^{2+} emission lines.

Fluorescence from O^+ ($3s\ ^4P^e$) at 53.9086–53.9853 nm and O^+ ($2s^{-1}\ ^2P^e$) at 53.7830–53.8318 nm was additionally measured in third order. It becomes apparent that almost all intensity in first order results from O^+ ($3s\ ^4P^e$), in accordance with the result of Flaig *et al.* (Ne^+(500 keV) on O_2) [23] but clearly at odds with the result of Yang and Cunningham [24] (fluorescence emission from a discharge lamp), who found fluorescence from O^+ ($2s^{-1}\ ^2P^e$) to be about half intense than fluorescence from O^+ ($3s\ ^4P^e$).

Fluorescence at 87.9 nm is dominantly emitted from O ($3s''\ ^3P^o$) fragments, since fluorescence from O ($3d'\ ^1P^o$, $^1D^o$, $^1F^o$) at 92.2 nm is already very weak and in consequence fluorescence from O ($4d'\ ^1P^o$,$^1D^o$,$^1F^o$) fragments at fluorescence wavelength 87.9 nm is negligible due to the higher main quantum number.

The most intensive emission, after quantum efficiency correction, is seen in the multiplet at 130.21685–130.60286 nm which is the long wavelength limit of the detectable fluorescence. The very low detection efficiency at these wavelengths implies large errors in the relative spectral quantum efficiency.

3.2 High resolution spectrum in the visible and near UV (340–605 nm)

The spectrum recorded in the visible and near UV spectral range after 2 keV electron impact on O_2 is displayed in Figure 3. Identified emission features are listed in Table 3 for fluorescence from excited neutral and singly ionised fragments and in Table 4 for fluorescence from singly ionised molecules. In order to present Table 3 in a condensed form finestructure multiplets are summarised, even if clearly separated in the spectrum. Observed emission lines are assigned according to Striganov and Sventitskii [16].

The spectral range from the cut off wavelength of the detector at 340 nm to 390 nm shows weak emission in the second negative band system of O_2^+ ($A\ ^2\Pi_u \rightarrow X\ ^2\Pi_g$). Band heads from Krupenie [17] are listed in Table 4 and are included in Figure 3 at the observed emission bands. The spectral range from 390 nm to 470 nm is characterised by line emission from excited singly ionised and neutral fragments. Molecular bands cannot be identified here. The spectral range from 470 nm up to 605 nm is finally dominated by fluorescence from the first negative band system of O_2^+ ($b\ ^4\Sigma_g^- \rightarrow a\ ^4\Pi_u$). As for the second negative band system, band heads taken from Krupenie [17] are included in Figure 3. A more detailed analysis of the first negative band system was carried out by Hughes and Ng [25] for proton impact on O_2.

Table 3. Observed electronic transitions in the visible/near UV with corresponding fluorescence wavelengths for dissociative ionisation and excitation. Fluorescence wavelengths are taken from Striganov and Sventitskii [16]. Finestructure multiplets are summarised.

Observed transition	Fluorescence wavelength
fluorescence from excited O^+ fragments	
$3p\ ^4S^o \rightarrow 3s\ ^4P^e$	371.275−374.949 nm
$3d\ ^4D^e \rightarrow 3p\ ^4D^o$	388.2197−388.315 nm
$3p'\ ^2P^o \rightarrow 3s'\ ^2D^e$	391.1960−391.2088 nm
$3p\ ^2P^o \rightarrow 3s\ ^2P^e$	391.9287−398.2719 nm
$3d\ ^4F^e \rightarrow 3p\ ^4D^o$	406.9634−409.418 nm
$4f\ ^4G^o \rightarrow 3d\ ^4F^e$	408.716−408.9295 nm
$3d\ ^4D^e \rightarrow 3p\ ^4P^o$	409.7260−412.0554 nm
$3d'\ ^2G^e \rightarrow 3p'\ ^2F^o$	418.5456−418.9788 nm
$4f'\ ^2H^o \rightarrow 3d'\ ^2G^e$	425.374−425.398 nm
$4f\ ^4F^o \rightarrow 3d\ ^4D^e$	427.552−428.296 nm
$4f\ ^4D^o \rightarrow 3d\ ^4P^e$	428.883−430.382 nm
$3p\ ^4P^o \rightarrow 3s\ ^4P^e$	431.7139−436.6896 nm
$4f'\ ^2D^o \rightarrow 3d'\ ^2D^e$	434.283 nm
$3p'\ ^2D^o \rightarrow 3s'\ ^2D^e$	434.7425−435.1269 nm
$4f'\ ^2F^o \rightarrow 3d'\ ^2D^e$	437.801−437.841 nm
$3p\ ^2D^o \rightarrow 3s\ ^2P^e$	441.4909−445.2377 nm
$3p'''\ ^6P^e \rightarrow 3s'''\ ^6S^o$	446.540−446.941 nm
$4f\ ^4D^o \rightarrow 3d\ ^2P^e$	446.628−446.632 nm
$4d\ ^4D^e \rightarrow 3p'\ ^2P^o$	446.932 nm
$4f'\ ^2D^o \rightarrow 3d'\ ^2P^e$	448.772−448.817 nm
$4f\ ^2D^o \rightarrow 3d\ ^2P^e$	448.948−449.125 nm
$3p'\ ^2F^o \rightarrow 3d'\ ^2D^e$	459.0971−459.6174 nm
$4f\ ^2F^o \rightarrow 3d\ ^2D^e$	460.211−461.367 nm
$3p\ ^4D^o \rightarrow 3s\ ^4P^e$	463.8854−467.6234 nm
$3d\ ^4D^e \rightarrow 3p\ ^4S^o$	485.649−486.495 nm
fluorescence from excited O fragments	
$4p\ ^5P^e \rightarrow 3p\ ^5S^o$	394.7301−394.7594 nm
$3s''\ ^3P^o \rightarrow 3p\ ^3P^e$	395.1987−395.4687 nm
$4p\ ^3P^e \rightarrow 3s\ ^3S^o$	436.830 nm
$5d\ ^5D^o \rightarrow 3p\ ^5P^e$	532.9101−533.0739 nm

Table 4. Observed emission in the first and second negative band system of O_2^+ in the visible/near UV. The respective band heads are tabulated in Krupenie [17].

Emission band	Fluorescence wavelength
2nd negative band system of O_2^+: $A\ ^2\Pi_u \rightarrow X\ ^2\Pi_g$	
various bands	340–390 nm
1st negative band system of O_2^+: $b\ ^4\Sigma_g^- \rightarrow a\ ^4\Pi_u$	
$\Delta v = 3$	495–501 nm
$\Delta v = 2$	519–530 nm
$\Delta v = 1$	553–564 nm
$\Delta v = 0$	581–602.5 nm

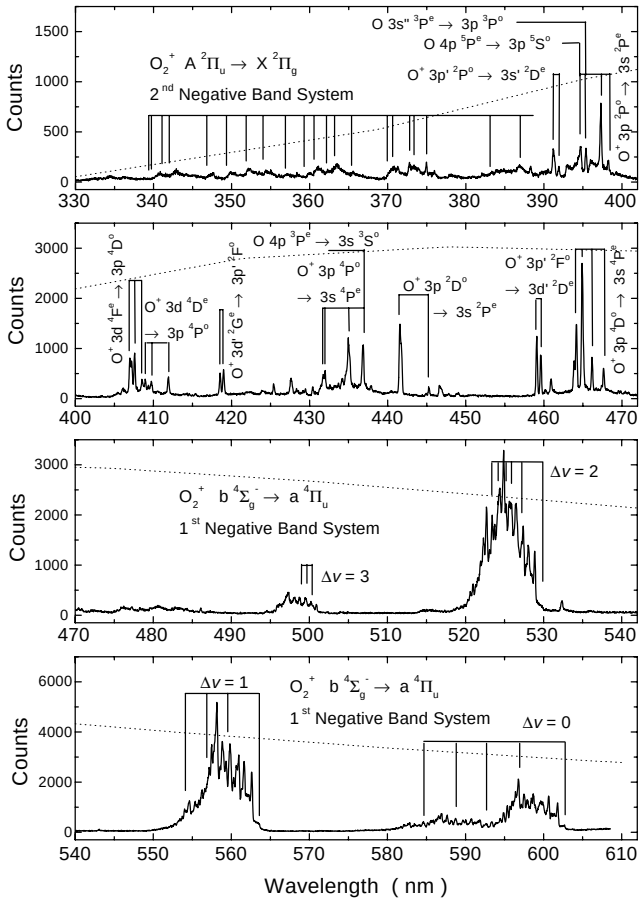

Fig. 3. The visible and near UV spectrum resulting from 2 keV electron impact on O_2. For the 1st and 2nd negative band system of O_2^+ the positions of band heads are included (*cf.* Tab. 4). Prominent emission lines from singly ionised and neutral fragments are assigned. All identified transitions are listed in Table 3. The relative spectral quantum efficiency of the detector [14] is illustrated by the dotted line (same scale in all graphs).

Intensities in Figure 3 are not corrected for the spectral detection efficiency, but the relative spectral quantum efficiency of the detector alone [14] is shown in Figure 3.

3.3 Emission cross-sections in the VUV

The emission cross-sections for dissociative ionisation and excitation processes leading to fluorescence in the VUV after collisions of protons and electrons with O_2 are displayed in Figures 4–6. For electron impact on O_2, they extend the energy range of the emission cross-sections of Ajello and Franklin [6] and of Morgan and Mentall [7], whose high energy limits are 400 eV and 300 eV, respectively, to 2 keV. For proton impact on O_2 individual emission cross-sections are presented for the first time.

The projectile velocities of the present experiment range from intermediate to high velocities, with the low proton velocities in the same order of magnitude as the classical velocities of the valence electrons in the oxygen molecule. High proton and low electron velocities

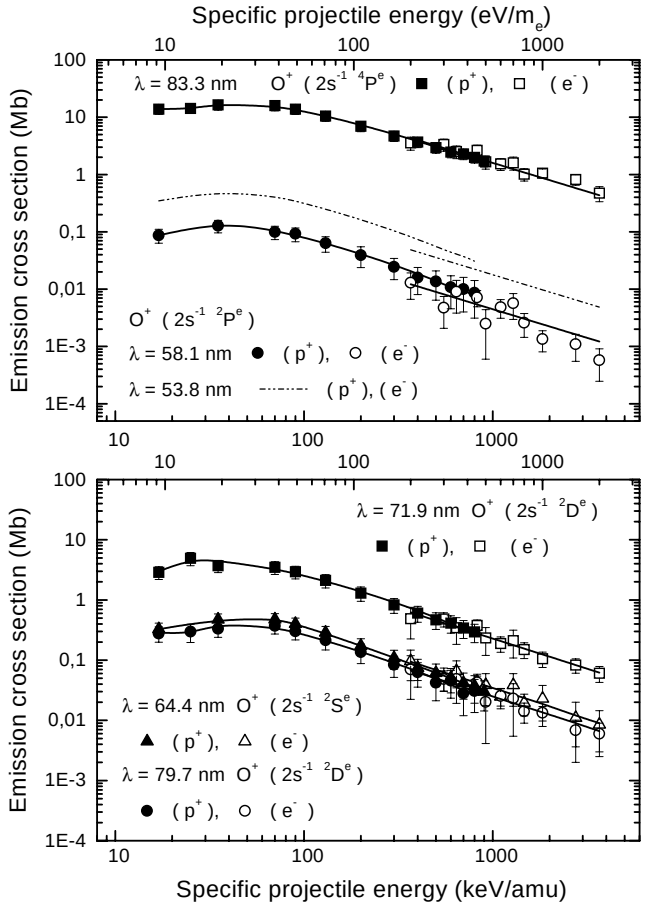

Fig. 4. Emission cross-sections for fluorescence lines resulting from dissociative $2s^{-1}$ ionisation by proton impact (compact symbols) and electron impact (open symbols) as function of the specific projectile energy (proportional to the square of the projectile velocity). The fitting functions are plotted as line graphs. The 53.8 nm line emission cross-section has been calculated from the 58.1 nm line emission cross-section, employing the 53.8/58.1 nm fluorescence branching ratio 4.0 [23]. Error bars include statistical errors only.

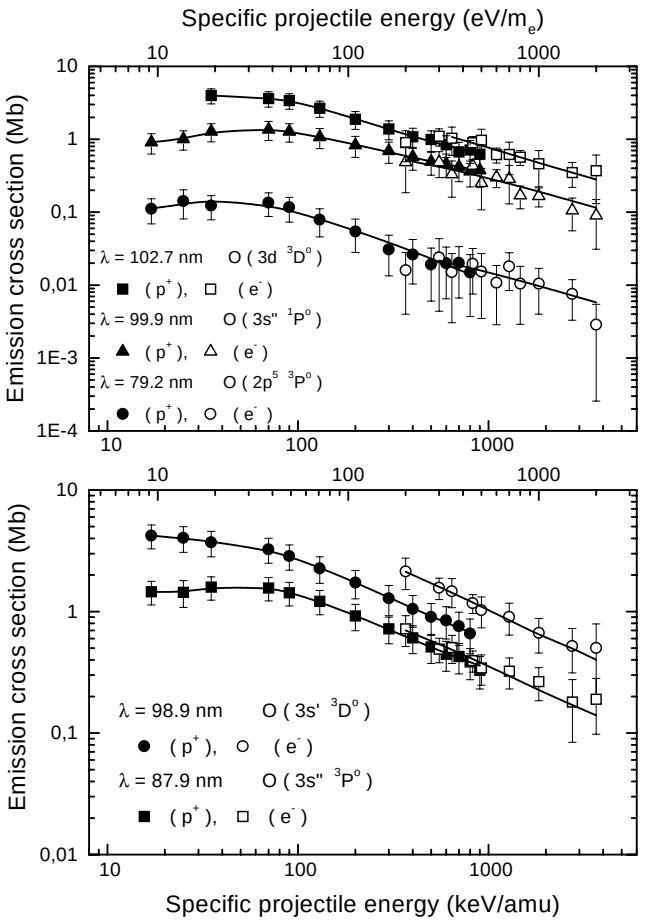

Fig. 5. Emission cross-sections for fluorescence lines resulting from dissociative excitation by proton impact (compact symbols) and electron impact (open symbols) as function of the specific projectile energy (proportional to the square of the projectile velocity). The fitting functions are plotted as line graphs. Error bars include statistical errors only.

allow a comparison of electron and proton collisions with O_2 at the same velocity. For the high electron velocities the first Born approximation can be considered as an adequate description of the ionisation and excitation process. At equivalent and sufficiently high projectile velocities the Bethe-theory [26] predicts identical emission cross-sections for fluorescence lines emitted after proton or electron impact. Such a behaviour is observed for all emission cross-sections in Figures 4–6 within the total error bars. Line graphs are fitted to the experimental data in order to guide the eye. For electron impact emission cross-sections, the fitting functions (Eqs. (7, 8)) have been derived from the asymptotic Bethe formulae [26]

$$\sigma = \frac{a}{E}\ln(bE) \quad \text{for optically allowed transitions} \qquad (7)$$

$$\sigma = \frac{c}{E} \quad \text{for optically forbidden transitions.} \qquad (8)$$

Since the Bethe-theory cannot be applied to proton impact on O_2 in the whole proton energy range, an inverse polynomial function has been fitted to the measured proton impact emission cross-sections (Eq. (9))

$$\sigma = a_0 + \frac{a_1}{x - x_0} + \frac{a_2}{(x - x_0)^2}\,. \qquad (9)$$

3.3.1 Dissociative ionisation into O^+ ($2s^{-1}\,{}^4P^e$), O^+ ($2s^{-1}\,{}^2D^e$), O^+ ($2s^{-1}\,{}^2S^e$) or O^+ ($2s^{-1}\,{}^2P^e$) fragments

Dissociative $2s^{-1}$ ionisation can produce four final ionic states, namely O^+ ($2s^{-1}$ $^4P^e$), O^+ ($2s^{-1}$ $^2D^e$), O^+ ($2s^{-1}$ $^2S^e$) and O^+ ($2s^{-1}$ $^2P^e$). The emission cross-sections for radiative decay of these ionic states are presented in Figure 4, the respective transitions in Table 1. The fluorescence line intensities have been analysed even for the very weak fluorescence lines at 58.1 nm and 79.7 nm (Fig. 2). From Table 1, it can be seen that the O^+ ($2s^{-1}\,{}^2P^e$) fragment does emit fluorescence at 53.8 nm and at 58.1 nm. With the spectral resolution achieved in the emission cross-section experiment the fluorescence at 53.8 nm could not be resolved from the much stronger

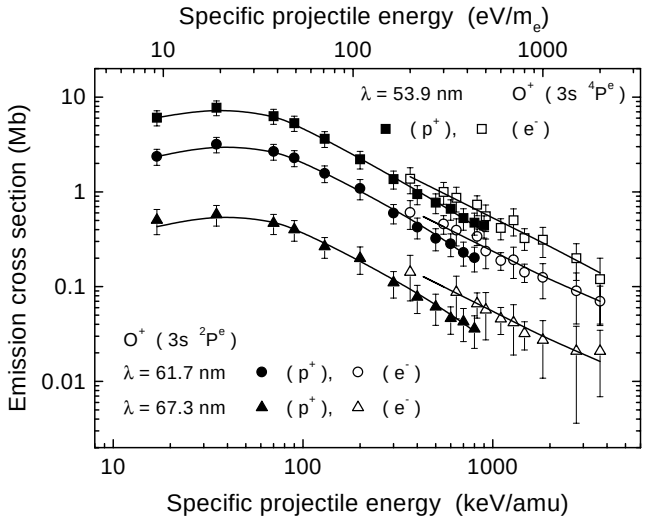

Fig. 6. Emission cross-sections for fluorescence lines resulting from dissociative ion excitation by proton impact (compact symbols) and electron impact (open symbols) as function of the specific projectile energy (proportional to the square of the projectile velocity). The fitting functions are plotted as line graphs. Error bars include statistical errors only.

fluorescence at 53.9 nm from O^+ ($3s\ ^4P^e$). Nevertheless, the emission cross-section of the 53.8 nm line in Figure 4 was derived from the emission cross-section at 58.1 nm using the intensity branching ratio $I(53.8\ \text{nm})/I(58.1\ \text{nm}) = 4.0$ [23]. For the branching ratio of the 79.7 nm to the 71.9 nm fluorescence lines emitted in transitions from O^+ ($2s^{-1}\ ^2D^e$) a mean value of 0.099 ± 0.013 was obtained from proton impact induced spectra. Electron impact induced spectra yield 0.109 ± 0.021. These ratios agree with the results for proton and electron impact on atomic oxygen: 0.109 ± 0.014 and 0.110 ± 0.021 (paper II [3]). Theoretical transition probabilities [30] yield a 79.7 nm line to 71.9 nm line branching ratio of 0.094.

Since no intensity could be measured for the only cascade transition known to us in the observed wavelength range, O^+ ($2s\ 2p^3\ 3s\ ^4S^o$) $\rightarrow O^+$ ($2s^{-1}\ ^4P^e$) at 74.0 nm [15], we consider cascades not to contribute to the population of the O^+ ($2s^{-1}$) states.

3.3.2 Dissociative excitation into O (3d ^{3}D°), O (3s′ ^{3}D°), O (3s″ ^{3}P°), O (3s″ ^{1}P°) or O (2p^5 ^{3}P°) fragments

After proton or electron impact dissociation of O_2 into a neutral excited fragment in the O ($3d\ ^3D^o$), O ($3s'\ ^3D^o$), O ($3s''\ ^3P^o$), O ($3s''\ ^1P^o$) or O ($2p^5\ ^3P^o$) state, fluorescence is emitted in the 102.7 nm line, the 98.9 nm line, the 87.9 nm line, the 99.9 nm line or the 79.2 nm line as listed in Table 1. The emission cross-sections are displayed in Figure 5. We note that no emission cross-section could be determined for the fluorescence multiplet from the O ($3s\ ^3S^o$) state at 130.4 nm, although it clearly appears in the high resolution spectra. Target density and detection efficiency with the 60-nm-blazed grating in the emission cross-section experiment did not permit reliable determination of emission cross-sections for fluorescence lines with wavelengths above 102.7 nm.

Excited neutral atomic states that lie energetically above the lowest ionisation threshold of atomic oxygen can also decay by autoionisation. For the investigated excited atomic states, autoionisation is considered with autoionisation factors AF, *i.e.* the probabilities of autoionisation from [28]: for O ($2p^5\ ^3P^o$) with fluorescence at 79.2 nm $AF = 0.51$ and for O ($3s''\ ^3P^o$) with fluorescence at 87.9 nm $AF = 0.46$.

The fluorescence lines emitted in possible cascade transitions have wavelengths above the examined visible spectral range, except the transition O ($3p''\ ^3D^e$) $\rightarrow$ O ($3s'\ ^3D^o$) at 382.5 nm [16]. No intensity was observed at this wavelength.

3.3.3 Dissociative ionisation into O$^+$ (3s ^{4}P^e) or O$^+$ (3s ^{2}P^e) fragments

Dissociative ion excitation was analysed for O^+ ($3s\ ^4P^e$) and O^+ ($3s\ ^2P^e$). These ionic states decay under emission of fluorescence lines at 53.9 nm and 61.7/67.3 nm, respectively (*cf.* Tab. 1). The emission cross-sections are shown in Figure 6. For the 67.3 nm line to 61.7 nm line branching ratio we obtain mean values of 0.182 ± 0.024 for proton impact and 0.232 ± 0.050 for electron impact. These values are in accord with each other within the error bars, but also with the results from proton and electron impact on atomic oxygen of 0.178 ± 0.023 and 0.243 ± 0.046 (paper II [3]) and from photoionisation of atomic oxygen of 0.19 ± 0.038 [4]. From theoretical transition probabilities calculated by Bell *et al.* [30] a branching ratio of 0.16 follows.

The visible spectrum in Figure 3 gives evidence that at least in the population of the excited ionic states O^+ ($3s\ ^4P^e$) and O^+ ($3s\ ^2P^e$), cascade transitions from higher excited ionic fragment states cannot be neglected. The cascade transitions O^+ ($3p\ ^4D^o$) $\rightarrow O^+$ ($3s\ ^4P^e$) at 463.9–467.6 nm, O^+ ($3p\ ^2D^o$) $\rightarrow O^+$ ($3s\ ^2P^e$) at 441.5–445.2 nm, O^+ ($3p\ ^4P^o$) $\rightarrow O^+$ ($3s\ ^4P^e$) at 431.7–436.7 nm and O^+ ($3p\ ^2P^o$) $\rightarrow O^+$ ($3s\ ^2P^e$) at 391.9–398.3 nm show up in the spectra. For these fluorescence lines only proton impact induced emission cross-sections for the unresolved 441.5 nm and 441.7 nm lines (Thomas and Bent [12]) are available. They range from 0.5 Mb at 40 keV proton energy to 0.025 Mb at 1 MeV, *i.e.* they amount to approximately 12% of the emission cross-sections for fluorescence emitted by the O^+ ($3s\ ^2P^e$) state. Radiative transitions into the O^+ ($3s$) states are the only decay channels for O^+ ($3p$). Therefore the emission cross-sections for fluorescence from the O^+ ($3s$) states correspond to dissociative ion excitation into O^+ ($3s$) states plus O^+ ($3p$) states.

3.3.4 Bethe-Fano plots of the emission cross-sections

Bethe-Fano plots of emission cross-sections, *i.e.* the products of emission cross-sections times specific projectile energies plotted against the logarithm of the specific

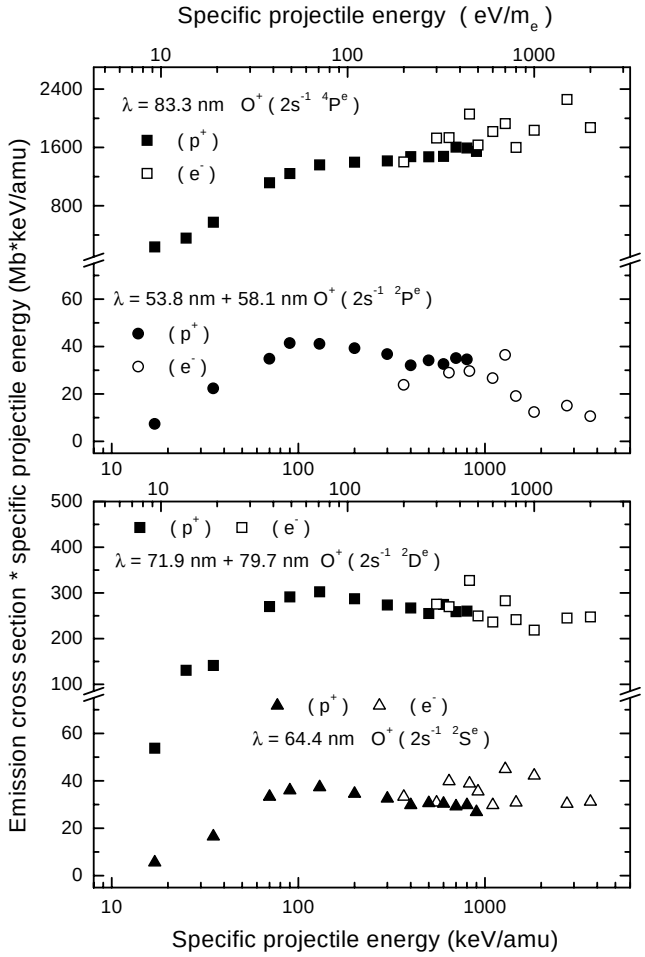

Fig. 7. Bethe-Fano plots of the emission cross-sections for fluorescence following dissociation into O^+ $(2s^{-1})$ fragments. Emission cross-sections of fluorescences lines originating from the same O^+ $(2s^{-1})$ state are summed.

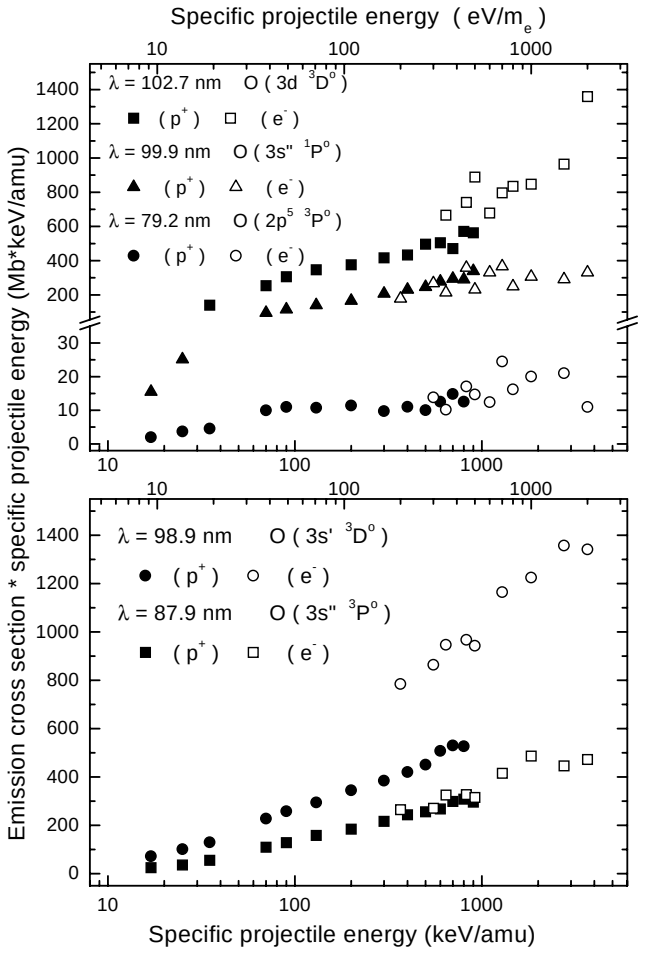

Fig. 8. Bethe-Fano plots of the emission cross-sections for fluorescence following dissociation into excited atomic fragments.

projectile energy [26], are characteristic for the dissociative ionisation or excitation process populating the upper state of the observed transition. Therefore Bethe-Fano plots of emission cross-sections of fluorescence lines originating from the same excited state are summed in order to characterise the excitation process. For all emission cross-sections in Figures 4–6, Bethe-Fano plots are illustrated in Figures 7–9.

Figure 7 presents the Bethe-Fano plots for the emission cross-sections of fluorescence lines emitted after dissociative $2s^{-1}$ ionisation. A different behaviour of the individual dissociative $2s^{-1}$ ionisation channels is observed. The Bethe-Fano plot for dissociative ionisation into O^+ $(2s^{-1}\ ^4P^e)$ by electron impact seems to show a linear increase, indicating an optically allowed transition (in accordance with the findings of Aarts and de Heer [9]). The Bethe-Fano plots connected with dissociative $2s^{-1}$ ionisation into O^+ $(2s^{-1}\ ^2D^e)$ and O^+ $(2s^{-1}\ ^2S^e)$ tend to a constant behaviour, which is a feature of optically forbidden transitions. The Bethe-Fano plot of the emission cross-sections for fluorescence from O^+ $(2s^{-1}\ ^2P^e)$ is seen to fall off as the electron energy is increased. The asymptotic Bethe formulae [26] do not provide a suitable reproduction of the latter case. Decreasing Bethe-Fano plots have been observed for the double ionisation of neon by proton and electron impact, where successive collisions of either the projectile with two target electrons or the ejected electron with a bound electron are considered as a reason [32].

The Bethe-Fano plots assigned to the dissociative excitation processes increase linearly (Fig. 8), in accordance with the asymptotic Bethe-formula for optically allowed transitions [26]. For the Bethe-Fano plot of the 79.2 nm line emission cross-sections, a linear rise cannot unambiguously be stated. The asymptotic behaviour of the Bethe-Fano plots for electron impact induced ion excitation in Figure 9 indicates an optically forbidden process.

Maxima for proton impact are observed for the dissociative $2s$-electron ionisation as for dissociative ion excitation. Even if the Bethe-theory cannot be applied to describe the p^+-O_2 collisions at the low proton velocities, the Bethe-Fano plots do nevertheless reveal information about the characteristics of the ionisation and excitation processes by elucidation of the projectile velocity dependence.

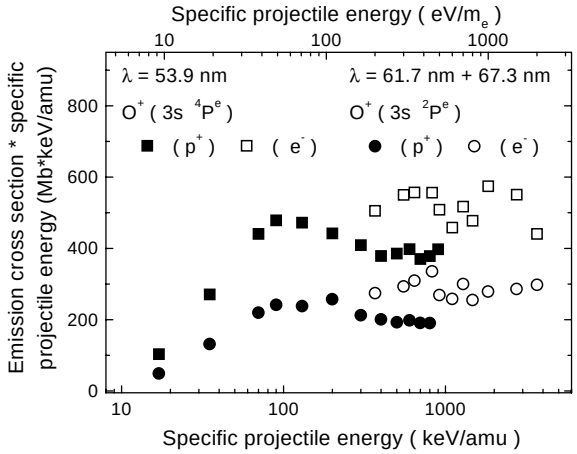

Fig. 9. Bethe-Fano plots of the emission cross-sections for fluorescence following dissociation into O^+ ($3s$) fragments. The emission cross-sections of fluorescences lines originating from the O^+ ($3s\ ^2P^e$) state are summed.

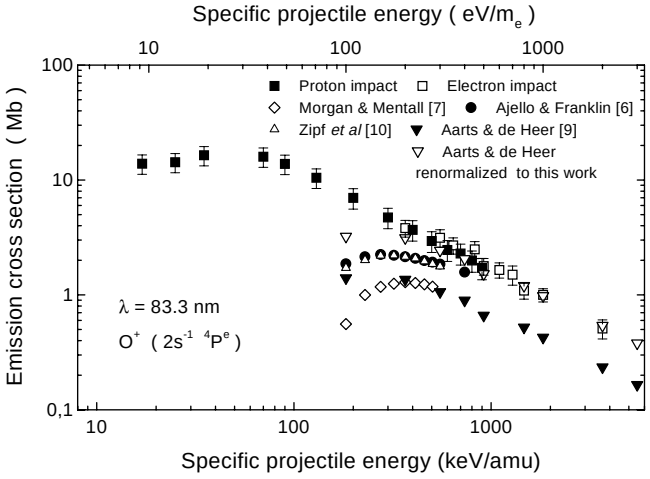

Fig. 10. Comparison of the 83.3 nm line emission cross-sections from this work with the results of the experiments of Aarts and de Heer [9], Morgan and Mentall [7], Ajello and Franklin [6] and Zipf *et al.* [10]. Error bars include statistical errors only.

3.3.5 Comparison of the absolute emission cross-sections

In previous studies of fluorescence emission resulting from electron impact on O_2, only the most intense line in the VUV spectrum at 83.3 nm had attracted interest. Our 83.3 nm line emission cross-sections are compared to experimental data of Aarts and de Heer [9], Ajello and Franklin [6], Morgan and Mentall [7] and Zipf *et al.* [10] in Figure 10. Only Aarts and de Heer [9] supply emission cross-sections above 400 eV electron energy. Our measurement yields the largest emission cross-sections. At energies below 500 eV our data also show a different energy dependence. This is demonstrated in Figure 10 by renormalising the data of Aarts and de Heer [9] to our data above 500 eV. The energy dependence of Aarts and de Heer [9] follows that of Ajello and Franklin [6] except for 100 eV. Their emission cross-sections agree very well with the Zipf *et al.* [10] results. Morgan and Mentall [7] agree well with Aarts and de Heer [9] but both deviate by roughly a factor 2 from Ajello and Franklin [6]. Our measurement supports Ajello and Franklin [6] within a factor of 1.3, as follows from an extrapolation of Ajello and Franklins [6] data with the energy dependence from Aarts and de Heer [9]. The larger deviation of a factor 1.7 at 200 eV is partly due to the difference in the energy dependence discussed above.

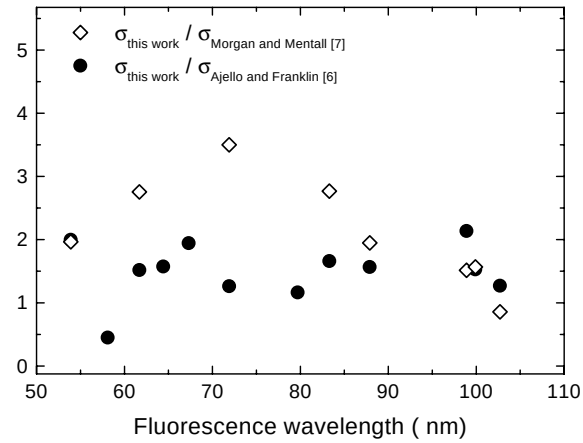

Fig. 11. Emission cross-section ratios derived from Table 5. Our results for 200 eV electron impact are divided by the emission cross-sections from Morgan and Mentall [7] and Ajello and Franklin [6].

Nevertheless, due to a lack of emission cross-sections for further electron energies, absolute emission cross-sections of fluorescence lines different from the 83.3 nm line have to be compared with the results of Ajello and Franklin [6] and Morgan and Mentall [7] at 200 eV electron energy. Table 5 gives a comparison of the emission cross-sections for 200 eV electron impact. The ratios of emission cross-sections from this work to the results of Morgan and Mentall [7] and of Ajello and Franklin [6] are illustrated in Figure 11. It is seen that the emission cross-sections presented here exceed the emission cross-sections of Ajello and Franklin [6] in the average by a factor of 1.5, just within the combined error bars of both experiments, especially since a factor of 1.3 was already deduced from the difference in energy dependence of the 83.3 nm line emission cross-sections of Aarts and de Heer [9] and our results (Fig. 10). The differences of our emission cross-sections to those of Morgan and Mentall [7] depend on fluorescence wavelength. At the fluorescence wavelength 53.9 nm as well as at fluorescence wavelengths above 85 nm a factor around 1.5 is also found. The larger deviation in between is possibly due to an error in the spectral quantum efficiency of Morgan and Mentall [7].

The above comparison is based on the originally published results. Van der Burgt *et al.* [22] recommended a renormalisation of the emission cross-sections due to a new electron impact induced cross-section for the Lyman-α line emission from H_2. The renormalisation is supported by the accurate emission cross-section measurement of Jans [20]. The renormalised emission cross-sections are also listed in Table 5. The results of Ajello and Franklin [6] are reduced

Table 5. Comparison of our emission cross-sections for 200 eV electron impact with the data from Ajello and Franklin [6] and from Morgan and Mentall [7]. Van der Burgt *et al.* [22] renormalised the original values from Ajello and Morgan, leading to smaller emission cross-sections which are included in brackets.

Fluorescence wavelength	Emission cross-sections in Mb for 200 eV electron impact on O_2		
	This work	Ajello and Franklin	Morgan and Mentall
53.9 nm	1.38	0.689 (0.61)	0.70 (0.43)
58.1 nm	0.013	0.029 (–)	– (–)
61.7 nm	0.61	0.399 (0.36)	0.22 (0.13)
64.4 nm	0.096	0.061 (–)	– (–)
67.3 nm	0.14	0.073 (–)	– (–)
71.9 nm	0.49	0.388 (0.35)	0.14 (0.09)
79.2 nm	0.016	– (–)	– (–)
79.7 nm	0.071	0.061 (–)	– (–)
83.3 nm	3.57	2.15 (1.92)	1.29 (0.78)
87.9 nm	0.72	0.46 (0.41)	0.37 (0.23)
98.9 nm	2.13	1.00 (0.89)	1.41 (0.86)
99.9 nm	0.49	0.318 (–)	0.31 (–)
102.7 nm	0.90	0.708 (0.63)	1.05 (0.64)

by 10%, whereas those of Morgan and Mentall [7] decrease by nearly a factor of 2.

Our normalisation relies on the 92.0 nm line emission cross-section of $\sigma = 1.17 \pm 0.06$ Mb supplied by Jans *et al.* [19] for 2 keV electron impact on Ar. Ajello *et al.* [29] report $\sigma = 1.20 \pm 0.17$ Mb. In consequence, the difference between emission cross-sections measured by ourselves and by Ajello and Franklin [6] cannot be attributed to the reference emission cross-section. A 92.0 nm line emission cross-section for 200 eV electron impact of Mentall and Morgan [27] was also renormalised by van der Burgt *et al.* [22] yielding $\sigma = 2.15$ Mb. Extrapolation, employing the energy dependence of the experimental 92.0 nm line emission cross-sections of Luyken *et al.* [31] ($\sigma = 1.29$ Mb at 2 keV), yields $\sigma = 0.27$ Mb at 2 keV. This cross-section is a factor 4 lower than those of Jans *et al.* [19] and Ajello *et al.* [29]. A similar factor is seen in the mean for the difference of Morgan and Mentalls [7] renormalised values to our data in Table 5, thus supporting the conclusion that Morgan and Mentall generally obtained too small emission cross-sections.

4 Summary

High resolution spectra are presented in the VUV and in the visible/near UV spectral region for 2 keV electron impact on O_2. They can substantially support fluorescence spectra analysis in experiments with limited spectral resolution, where close lying fluorescence lines cannot be separated. In the case of the emission cross-section measurement, fluorescence intensities at wavelengths 83.3 nm, 53.9 nm and 87.9 nm could be related to transitions from excited dissociation fragments O^+ ($2s^{-1}$ $^4P^e$), O^+ ($3s$ $^4P^e$) and O ($3s''$ $^3P^o$), respectively, because overlapping fluorescence lines were seen to have negligible intensities in the high resolution VUV spectrum. The combination of spectra in both spectral ranges can provide complementary information, like a contribution to the VUV fluorescence of O^+ ($3s$ $^4P^e$) and O^+ ($3s$ $^2P^e$) from cascade population was revealed in the visible spectra.

Absolute emission cross-sections for electron impact (0.2–2 keV) and proton impact (17–800 keV) are presented. Electron impact emission cross-sections for line emission at 83.3 nm are in agreement with the results of Ajello and Franklin [6] and Zipf *et al.* [10] at high electron energies, but consequently are larger than the emission cross-sections of Morgan and Mentall [7] and Aarts and de Heer [9]. A comparison of the other line emission cross-sections with previously published data can only be carried out at 200 eV electron energy, where our results are larger than those of Ajello and Franklin [6] by an average factor 1.5.

Emission cross-sections have so far been limited to electron impact with energies below 400 eV, except for the 83.3 nm line. In the present study the energy range has been extended to 2 keV, where a test of the emission cross-section energy dependence with respect to the Bethe-theory becomes feasible. Emission cross-sections for proton impact on O_2 are presented for the first time, beside the 441.5/441.7 nm emission cross-sections [12].

The presented results are part of an extensive study of fluorescence emission resulting from proton and electron impact and from VUV photon absorption with molecular and atomic oxygen gas targets (paper II [3–5]).

The experiments have been funded by the Deutsche Forschungsgemeinschaft (DFG). We are indebted to A. Werner for all the work he did in the preparation of these experiments. The technical assistance of G. Trylat in setting up the experiment and running the van de Graaff Accelerator is greatly

appreciated. Thanks to G. Mentzel and H. Liebel, who supported the measurements of the highly resolved spectra. The use of the detector for the visible and near UV spectral range of the workgroup of H. Schmoranzer at the Universität Kaiserslautern is gratefully acknowledged.

References

1. J.A. Whalen, R.R. O'Neil, R.H. Picard, G.P. Anderson, H.S. Muench, R.E. Good, C.R. Philbrick, W. Swider, *Handbook of geophysics and the space environment*, edited by A.S. Jursa (Air Force Geophysics Laboratory, 1985).
2. P.D. Feldman, D.E. Anderson Jr, R.R. Meier, E.P. Gentieu, J. Geophys. Res. **86**, 3583 (1981).
3. O. Wilhelmi, K.-H. Schartner, Eur. Phys. J. D **11**, 45 (2000)
4. O. Wilhelmi, G. Mentzel, B. Zimmermann, K.-H. Schartner, H. Liebel, H. Schmoranzer, B.M. McLaughlin, Phys. Rev. A **60**, 3702 (1999).
5. H. Liebel, M. von Kröger, H. Schmoranzer, O. Wilhelmi, B. Zimmermann, K.-H. Schartner, Phys. Lett. A (submitted, 1999).
6. J.M. Ajello, B. Franklin, J. Chem. Phys. **82**, 2519 (1985).
7. H.D. Morgan, J.E. Mentall, J. Chem. Phys. **78**, 1747 (1983).
8. Y. Itikawa *et al.*, J. Phys. Chem. Ref. Data **18**, 23 (1989).
9. J.F.M. Aarts, F.J. de Heer, Physica **56**, 294 (1971).
10. E.C. Zipf, W.W. Kao, R.W. McLaughlin, Chem. Phys. Lett. **118**, 591 (1985).
11. W. Sroka, Z. Naturforsch. **23a**, 2004 (1968).
12. E.W. Thomas, G.D. Bent, J. Phys. B: At. Mol. Opt. Phys. **1**, 233 (1968).
13. H. Liebel, F. Vollweiler, Universität Kaiserslautern, private communication.
14. M. Reisser, Diplomarbeit, Universität Kaiserslautern, 1988.
15. R.L. Kelly, J. Phys. Chem. Ref. Data **16** (Suppl. 1), 85 (1987).
16. A.R. Striganov, N.S. Sventitskii, *Tables of spectral lines of neutral and ionized atoms* (IFI/Plenum, New York - Washington, 1968).
17. P.H. Krupenie, J. Phys. Chem. Ref. Data **1**, 423 (1972).
18. H. Pauly, in *Atomic and molecular beam methods*, edited by G. Scales (Oxford University Press, 1988).
19. W. Jans, B. Möbus, M. Kühne, G. Ulm, A. Werner, K.-H. Schartner, Phys. Rev. A **55**, 1890 (1997).
20. W. Jans, Ph.D. thesis, Technische Universität Berlin, 1993.
21. R. Hippler, K.-H. Schartner, J. Phys. B: At. Mol. Opt. Phys. **7**, 1167 (1974); Ar 3s-electron ionization cross-sections multiplied with 1.3 (private communication).
22. P.J.M. van der Burgt, W.B. Westerveld, J.S. Risley, J. Phys. Chem. Ref. Data **18**, 1757 (1989).
23. H.J. Flaig, K.-H. Schartner, E. Träbert, P.H. Heckmann, Phys. Scripta **31**, 255 (1985).
24. F. Yang, A.J. Cunningham, J. Quant. Spectrosc. Radiat. Transfer **49**, 53 (1993).
25. R.H. Hughes, D.K.W. Ng, Phys. Rev. A **136**, 1222 (1964).
26. M. Inokuti, Rev. Mod. Phys. **43**, 297 (1971).
27. J.E. Mentall, H.D. Morgan, Phys. Rev. A **14**, 954 (1976).
28. R.R. Laher, F.R. Gilmore, J. Phys. Chem. Ref. Data **19**, 277 (1990).
29. J.M. Ajello, G.K. James, B. Franklin, S. Howell, J. Phys. B: At. Mol. Opt. Phys. **23**, 4355 (1990).
30. K.L. Bell, A. Hibbert, R.P. Stafford, B.M. McLaughlin, Phys. Scripta **50**, 343 (1994).
31. B.F.J. Luyken, F.J. de Heer, R.C. Baas, Physica **61**, 200 (1972).
32. M. Eckhardt, K.-H. Schartner, Z. Phys. A **312**, 321 (1983).